Characterization of the ScAlMgO4 cleaving layer by X-ray crystal truncation rod scattering

doi: 10.1063/1.5031024

Characterization of the $ScAlMgO_4$ cleaving layer by X-ray crystal truncation rod scattering

Takashi Hanada, Hiroo Tajiri, Osami Sakata, Tsuguo Fukuda, and Takashi Matsuoka

Citation: Journal of Applied Physics **123**, 205305 (2018); doi: 10.1063/1.5031024
View online: https://doi.org/10.1063/1.5031024
View Table of Contents: http://aip.scitation.org/toc/jap/123/20
Published by the American Institute of Physics

Characterization of the $ScAlMgO_4$ cleaving layer by X-ray crystal truncation rod scattering

Takashi Hanada,[1] Hiroo Tajiri,[2] Osami Sakata,[3] Tsuguo Fukuda,[4] and Takashi Matsuoka[1]
[1]*Institute for Materials Research, Tohoku University, Sendai 980-8577, Japan*
[2]*Japan Synchrotron Radiation Research Institute (JASRI), Hyogo 679-5198, Japan*
[3]*Synchrotron X-ray Station at SPring-8, National Institute for Materials Science, Hyogo 679-5148, Japan*
[4]*Fukuda Crystal Laboratory, Sendai 989-3204, Japan*

(Received 27 March 2018; accepted 6 May 2018; published online 24 May 2018)

$ScAlMgO_4$—easily cleaved in *c*-plane—forms a natural superlattice structure of a ScO_2 layer and two $Al_{0.5}Mg_{0.5}O$ layers stacking along *c*-axis. $ScAlMgO_4$ is one of the $RAMO_4$-type layered multicomponent oxides and a promising lattice-matching substrate material for InGaN and ZnO. Identification of the topmost layer and the surface atomic structure of the cleaved $ScAlMgO_4$ (0001) are investigated by the X-ray crystal truncation rod scattering method. It is confirmed that $ScAlMgO_4$ is cleaved between the two $Al_{0.5}Mg_{0.5}O$ layers. The two parts separated at this interlayer are inversion symmetric to each other and without surface charge. This prevents parallel-plate-capacitor-like electrostatic force during the cleavage. Two different mechanisms are proposed for the two types of cleavage caused by the impact of a wedge and by the in-plane stress due to an overgrown thick GaN film. It is also revealed that about 10%–20% of the topmost O atoms are desorbed during a surface cleaning at 600 °C in ultra-high vacuum. Surface observations using reflection high-energy electron diffraction are possible only after the high-temperature cleaning because the electrical conduction caused by the oxygen deficiency prevents the charge-up of the insulating sample. *Published by AIP Publishing*. https://doi.org/10.1063/1.5031024

I. INTRODUCTION

GaN-based light-emitting devices and transistors with high-power and high-frequency capabilities will be crucial devices for the future sustainable society. The quest for better substrate materials for them is still important because there are several restrictions for the use of a bulk GaN substrate such as quality, quantity, and cost. Al_2O_3 substrates are widely used for the GaN-based devices. Compared to Al_2O_3, $ScAlMgO_4$, with a lattice constant of about 3.25 Å along *a*-axis, has small *c*-plane lattice-[1–3] and thermal-expansion-[3,4] mismatches to GaN. Furthermore, bulk $ScAlMgO_4$ over 2 in. in diameter can be grown by the Czochralski method.[4] The first application of $ScAlMgO_4$ as a substrate for GaN growth was performed by Hellman *et al.* using the molecular beam epitaxy.[5] Then, it was used for ZnO epitaxy by the pulsed laser deposition[6] and a ZnO-based LED.[7] Recently, it has been confirmed that the $ScAlMgO_4$ substrate is stable enough in the reactive atmosphere of the metalorganic vapor-phase epitaxy (MOVPE), which is used for the commercial device fabrication, of GaN[4,8] and InGaN.[8] Also, a GaN-based LED on $ScAlMgO_4$ has been demonstrated.[9]

The crystal structure of $ScAlMgO_4$ is trigonal with ABCABC… stacking sequence of *c*/3 unit along *c*-axis. The *c*/3 unit consists of a rocksalt(111)-like ScO_2 layer and two h-BN-like $Al_{0.5}Mg_{0.5}O$ (Al/MgO) layers stacking along *c*-axis,[2,3] as shown in Fig. 1. $ScAlMgO_4$ is easily cleaved along the *c*-plane.[5,6] Thus, atomically flat *c*-plane substrates with large wafer diameter can be easily prepared by only cleavage without polishing.[4] This leads to a drastic cost reduction in the substrate fabrication. The residual strain of GaN on $ScAlMgO_4$ is smaller than that on sapphire because mismatch of the thermal-expansion coefficient is smaller.[3,4] On the other hand, the small thermal conductivity of $ScAlMgO_4$ is a disadvantage for device operations.[8,9] However, a $ScAlMgO_4$ substrate is removed from a halide-vapor-phase-epitaxy-grown thick GaN film by a self-cleavage, which releases the strain energy and wafer bowing induced by the thermal-expansion mismatch.[10] Therefore, $ScAlMgO_4$ is considered to be a promising substrate for the thick GaN growth.

However, there is neither experimental nor theoretical study on the identification of the topmost layer and the atomic structure of the cleaved surface. The bond lengths shown in Fig. 1 are calculated from the bulk structure data at 323 K.[3] The bond length between the neighboring Al/MgO layers is 0.3 Å longer than those of the other two kinds of bonds between Al/Mg and O as shown in Fig. 1. This suggests that the bonding between the neighboring Al/MgO layers is weak. However, the bond-length difference is not so large compared with that of h-BN and graphite, whose length ratio of the inter-layer and intra-layer bonds is about 2.3. Moreover, the bond density between the neighboring Al/MgO layers is twice of that between an Al/MgO layer and neighboring ScO_2 layer. Therefore, it is not apparent whether $ScAlMgO_4$ is cleaved between the neighboring Al/MgO layers or between the Al/MgO layer and the ScO_2 layer from the point of strength of the bonding between the neighboring layers.

In the present paper, the structure of the topmost layer of a cleaved $ScAlMgO_4$ before and after cleaning at 600 °C in ultra-high vacuum (UHV) is investigated by X-ray crystal-truncation rod (CTR) scattering method[12–14] because the substrate surface structure is an important information to

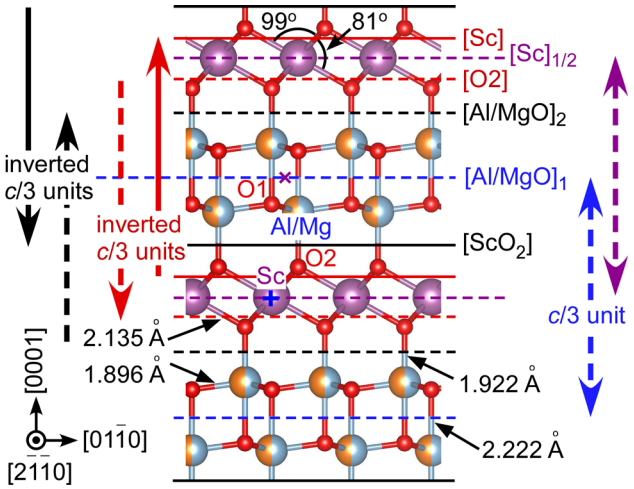

FIG. 1. Cross-sectional atomic-structure of $ScAlMgO_4$ in *a* plane. Six kinds of truncations parallel to *c*-plane are shown by horizontal lines. Al/Mg consists of 50% Al and 50% Mg. In the $[Sc]_{1/2}$ model, both of the upper and lower separated layers accept 50% of the Sc atoms.

design the growth procedure of high-quality films. It is revealed that $ScAlMgO_4$ is cleaved between the two Al/MgO layers and about 10%–20% of the topmost O atom is desorbed during the thermal cleaning in UHV.

II. EXPERIMENTAL METHOD

Bulk $ScAlMgO_4$ was grown by Czochralski method in Fukuda Crystal Laboratory. X-ray CTR scattering of a cleaved $ScAlMgO_4$ was measured by using a general-purpose UHV chamber mounted on a diffractometer at BL13XU,[15] SPring8. A thick plate of $ScAlMgO_4$ was cleaned by organic solvents and purified water. A *c*-plane $ScAlMgO_4$ sample with the thickness of about 0.2 mm was cleaved in air from the plate by softly hitting a razor blade attached at an edge of the plate. Care was taken to prevent the razor blade from touching the cleaved surface. Then, the sample was loaded into the pre-evacuation chamber without any treatment and the evacuation was started within 7 min after the cleavage. The as-cleaved surface was strongly charged by the electron beam of reflection high-energy electron diffraction (RHEED) in the UHV chamber. Therefore, it is presumably difficult to investigate the as-cleaved surface by charged beams in a conventional condition. The cleaved $ScAlMgO_4$ surface was cleaned in UHV at 600 °C for 18 min to remove adsorbates such as a hydrocarbon adsorbed in the air. After cleaning, an RHEED pattern of a 1×1 surface appeared. Both before and after cleaning, CTR scattering intensities of the cleaved $ScAlMgO_4$ were measured at 298 K with X-ray energy of 12.4 keV.

III. RESULTS AND DISCUSSION

A. Identification of the topmost layer of the cleaved $ScAlMgO_4$

An RHEED pattern of the cleaned surface was observed at the incident azimuth of −0.08° from [2$\bar{1}\bar{1}$0], the glancing angle of 3°, and the electron energy of 15 keV as shown in Fig. 2. Three surface reflection spots on the 0$\bar{1}$, 00, and 01 rods appear at the intersections with the Ewald sphere, where surface *hk* rod is along *l* of the $hk\overline{h+k}l$ Miller-Bravais indices. The simulated positions of the spots are indicated by green circles in the right pattern. To take the refraction of the electron beam at the surface into account, the mean inner potential of $ScAlMgO_4$ is assumed to be 16 eV. Other weak spots along the rods appear at the intersections with Kikuchi lines, whose simulated positions are shown by green lines. These weak spots do not fully correspond with the array of bulk Bragg reflections (yellow dots), which is frequently observed from a rough surface with three-dimensional structures. The observed RHEED pattern indicates that the surface is still flat after cleaning.

The CTR scattering intensities along the 01$\bar{1}l$, 10$\bar{1}l$, and 11$\bar{2}l$ rods for the cleaved $ScAlMgO_4$ before (×) and after (dot) cleaning are shown in Fig. 3 as a function of the reciprocal-lattice index *l*. The lattice constants of the $ScAlMgO_4$ sample are 3.246 Å and 25.102 Å in *a* and *c* directions, respectively, which are obtained from the bulk Bragg peak positions. The measured intensities are corrected to be proportional to $|F|^2$,[16,17] where *F* is the crystal structure factor of the bulk truncated $ScAlMgO_4$ and its surface layers. To compare the calculated intensity $|F|^2$ with the observed intensity, the latter is divided by a scale factor *s* common to all rods. In Fig. 3, *s* for the optimized structure, which will be described in Sec. III B, is used.

In this section, the cleavage position is identified by the characteristic deep dips observed at $l = 0.8$, 4.0, 9.5, and 11.5 along the 01$\bar{1}l$ rod and at $l = 3.5$, 4.7, and 10.8 along the 11$\bar{2}l$ rod in the CTR curves. The dashed lines in Fig. 3 are the calculated intensities for the ideal truncation at the $[Al/MgO]_1$ position shown in Fig. 1. The fractional atomic position *z* and anisotropic mean-square displacement (MSD) parameters are fixed at the values of bulk $ScAlMgO_4$ measured at 323 K by Simura *et al.*[3] Among the six truncation surfaces shown in the atomic structure in Fig. 1, only the $[Al/MgO]_1$ truncation fairly reproduces the deep dips observed in the CTR spectra (see the supplementary material for the calculated intensities other than the $[Al/MgO]_1$ truncation). As shown in Fig. 1, the *c*/3 units of the $[Al/MgO]_1$ and $[Sc]_{1/2}$ truncation models have inversion centers at the marks + and ×, respectively. The $[Sc]_{1/2}$ model is truncated at the Sc layer of half occupancy. Both the models produce deep dips. However, calculated positions of the deep dips for the $[Sc]_{1/2}$ truncation are apparently in contradiction to the observation and this model is excluded. The models without any inversion symmetry in their *c*/3 unit do not reproduce

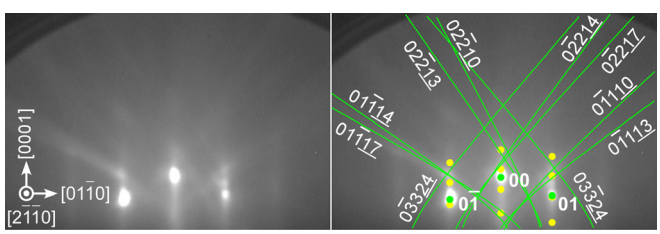

FIG. 2. RHEED pattern of the clean $ScAlMgO_4(0001)$ 1×1 surface at [2$\bar{1}\bar{1}$0] azimuth. Calculated positions of the cross section between Ewald sphere and the 0$\bar{1}$, 00, and 01 surface rods (green dot), some bulk Bragg reflections along the rods (yellow dot), and some bright Kikuchi lines (green lines) are overlaid in the right pattern.

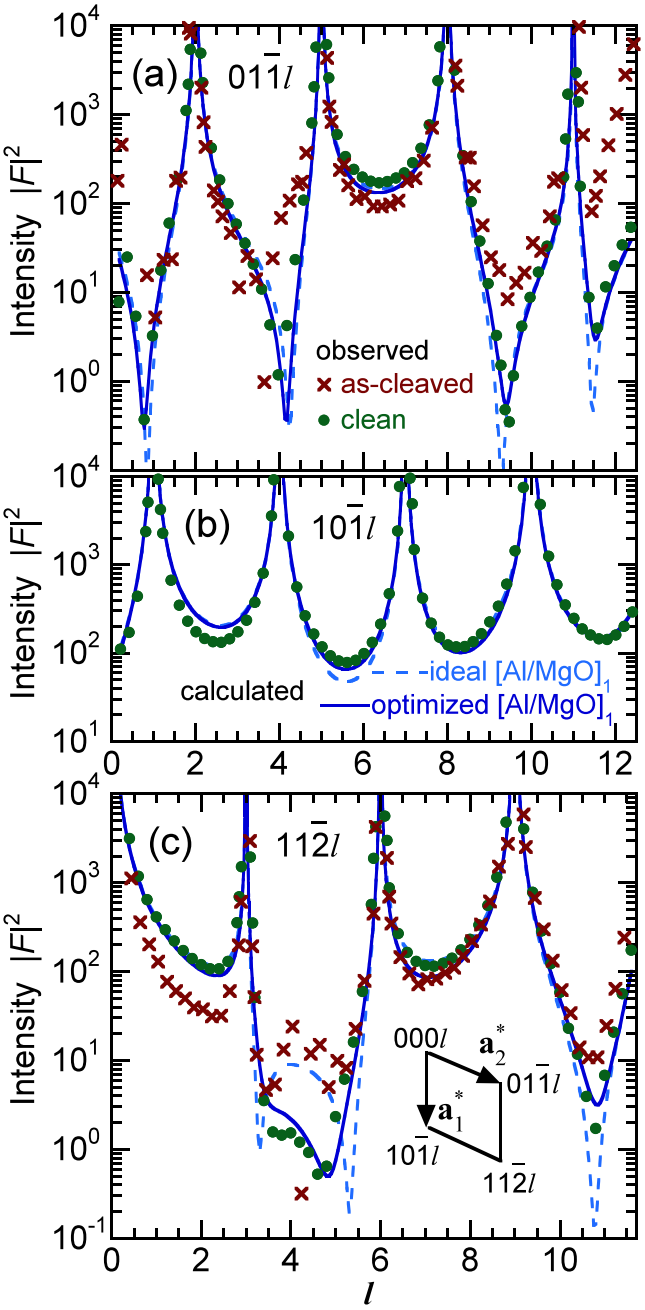

FIG. 3. Observed CTR scattering intensities of the as-cleaved (×) and the clean (dot) $ScAlMgO_4(0001)$ surface along with calculated curves for the ideal (dashed line) and optimized (solid line) $[Al/Mg\text{-}O]_1$ truncation models. The optimized parameters are shown in Tables I–III. Inset in (c) shows the basis vectors of the c-plane reciprocal lattice and positions of the rods.

the deep dips observed in the $01\bar{1}l$ and $11\bar{2}l$ rods and these models are also excluded.

In order to discuss the relation between the appearance of the deep dips and the inversion symmetry, kinematical calculation method of the CTR scattering intensity is briefly reviewed as below.[12] The structure factor of a truncated bulk $ScAlMgO_4$ and its surface layer are represented as

$$F = F_{u/3}G + F_s, \tag{1}$$

where $F_{u/3}$ is the structure factor of a $c/3$ bulk unit of $ScAlMgO_4$, F_s is the structure factor of a surface layer, and G comes from the stacking of the $c/3$ units as described later. $F_{u/3}$ is calculated using the parameters of seven atoms in the $c/3$ unit as

$$F_{u/3} = \sum_{j=1}^{7} f_j e^{-M_j} \exp\left[2\pi i(hx_j + ky_j + lz_j)\right], \tag{2}$$

where f_j is the atomic scattering factor[18,19] of atom j (see the supplementary material), and x_j, y_j, and z_j are the fractional coordinates of atom j in the unit cell. Imaginary part of f_j is usually very small.[19] The second factor in the right-hand side of Eq. (2) represents the reduction of the scattering factor owing to the random displacements of atom j, and M_j is expressed as

$$M_j = \frac{8\pi^2}{3a^2}(h^2 + hk + k^2)U_{11j} + \frac{2\pi^2}{c^2}l^2U_{33j}, \tag{3}$$

where U_{11j} and U_{33j} are MSD parameters of atom j perpendicular and parallel to c-axis, respectively. F_s is similarly expressed with $F_{u/3}$ using surface atoms, except that atomic scattering factors are multiplied by the atomic occupancy ratio. Finally

$$G = \sum_{j=-\infty}^{0} \exp\left\{\left[\frac{2\pi}{3}i(-h+k+l) + \eta\right]j\right\} \tag{4}$$

is a summation of phase factors of semi-infinitely stacking $c/3$ units in the ABCABC… sequence as shown in Fig. 4, where j is from the infinitely deep unit to the topmost unit ($j = 0$). In Eq. (4), η is a small positive value ($5.8 \times 10^{-4}/l$ for $ScAlMgO_4$ at skew-symmetric geometry and X-ray energy of 12.4 keV) due to the absorption of X-ray going in and out through the $c/3$ unit of $ScAlMgO_4$. The summation due to the two-dimensional periodicity within the c plane is not explicitly shown in G. Instead of this, h and k are limited to a pair of integers. On the other hand, owing to the truncation of the periodicity along c axis at the surface, G is not zero even at non-integer l and

$$|G|^2 = \frac{1}{1 + e^{-2\eta} - 2e^{-\eta}\cos\left[\frac{2\pi}{3}(-h+k+l)\right]}. \tag{5}$$

The right-hand side of Eq. (5) has sharp peaks of Bragg reflections as shown in the CTR spectra in Fig. 3 when $-h+k+l$ is a multiple of three and the cosine in Eq. (5) is

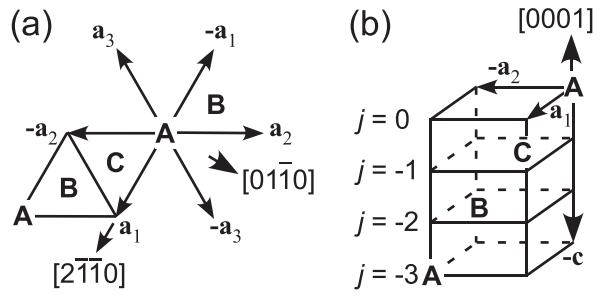

FIG. 4. Illustration of c-plane lattice vectors (a) and stacking sequence along c-axis (b) of $ScAlMgO_4$. A, B, and C represent shift of an identical site, for instance Sc site, in the successive $c/3$ units.

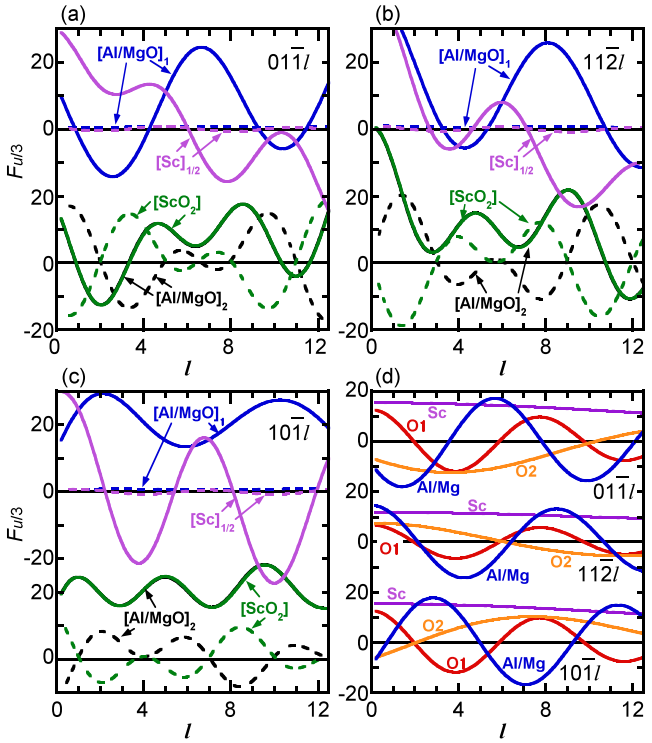

FIG. 5. Real (solid line) and imaginary (dashed line) parts of the $01\bar{1}l$ (a), $11\bar{2}l$ (b), and $10\bar{1}l$ (c) structure factors of $c/3$ unit for the [Al/Mg-O]$_1$, [Sc]$_{1/2}$, [ScO$_2$], and [Al/Mg-O]$_2$ truncations. The atomic components of the real part of the structure factor for the [Al/Mg-O]$_1$ truncation are also shown in (d).

unity. If the surface can be approximated as an ideally truncated bulk structure, F_s in Eq. (1) is zero and the scattering intensity is proportional to

$$|F|^2 = |F_{u/3}|^2 |G|^2. \tag{6}$$

$|G|^2$ is common for all truncation models and always greater than 1/4.

The appearance of the deep dips can be related to the inversion symmetry as follows. Figures 5(a)–5(c) show the real (solid lines) and imaginary (dashed lines) parts of $F_{u/3}$ for the $01\bar{1}l$, $11\bar{2}l$, and $10\bar{1}l$ rods, respectively. In the cases of the [Al/MgO]$_1$ and [Sc]$_{1/2}$ truncations, the imaginary part of $F_{u/3}$ is very small owing to the inversion symmetry if the inversion center (+ or × in Fig. 1) of these models is set to be the origin of the atomic coordinates in Eq. (2). A shift of the origin does not change the norm of $F_{u/3}$ and the intensity. As a result, the zero-crossing points of the real part of $F_{u/3}$ correspond to the positions of the deep dips in Fig. 3. On the other hand, in the cases of other four truncation models in Fig. 1, the real and imaginary parts of complex $F_{u/3}$ must coincidently approach to zero, which rarely happens, to form a dip. In Figs. 5(a)–5(c), where the origin of the atomic coordinates is set at Sc atom, there is no point where the real and imaginary parts of $F_{u/3}$ coincidently approach to zero for the [Al/MgO]$_2$ and [ScO$_2$] truncations.

Figure 5(d) shows the components constructing the real part of $F_{u/3}$ due to the respective symmetric pairs of atoms in the $c/3$ unit for the [Al/MgO]$_1$ model. The curves for Sc in Fig. 5(d) correspond to $f_{Sc}e^{-M_{Sc}}$ in Eq. (2) because Sc is located at the origin. The real part of $F_{u/3}$ can be negative when the Al/Mg component is negative and the O1 and O2 components are not out of phase with it. However, the latter components are out of phase along the $10\bar{1}l$ rod and no deep dip is observed in its CTR curve. If Sc is replaced with much heavier atoms like In,[1,11] the real part of $F_{u/3}$ for the [Al/MgO]$_1$ truncation does not cross zero and the characteristic deep dips in the CTR curves disappear. Therefore, inversion symmetry is not a sufficient condition for the appearance of the deep dips in CTR curves. It is not a necessary condition either; a dip appears in a CTR curve of zincblende type GaAs(001) without inversion symmetry.[14] This is because diamond type Ge has an inversion center at the center of a bond and GaAs has the same structure with Ge except for the slightly different atomic numbers between the nearest neighbors (See Fig. 4 of Ref. 14). As for the present analysis, however, inversion symmetry is surely the key factor.

The [Al/MgO]$_2$ and [ScO$_2$] truncations coincidently appear after the separation. Their $c/3$ units have structures inverted each other and their $F_{u/3}$s are each other's complex conjugate as shown in Figs. 5(a)–5(c). As a result, it is difficult to distinguish the pair of surfaces by CTR method unless the surfaces are reconstructed to some extent. The same is true between the [Sc] and [O$_2$] truncations.

The CTR scattering intensities of the as-cleaved surface (×) and the cleaned surface (dot) in Fig. 3 have the low-intensity dips in the identical hollows between the neighboring Bragg peaks along the 01 $\bar{1}l$ and 11 $\bar{2}l$ rods. Moreover, the positions of the dips are reproduced only by the [Al/MgO]$_1$ truncation. This suggests that the as-cleaved surface is also truncated at [Al/MgO]$_1$ and covered with adsorbates in the air, which moderately modify the CTR curves. Therefore, we believe that ScAlMgO$_4$ is cleaved between the two Al/MgO layers and the surface is substantially retained after the thermal cleaning.

B. Details of the cleaved surface structure after thermal cleaning

To refine the agreement between the observed and calculated CTR curves, parameters of the [Al/MgO]$_1$ truncation model listed in Tables I and II are optimized. In these calculations, the additional surface Al/MgO layer is placed on top of the [ScO$_2$] bulk truncation. To obtain the optimized parameters, R-factor defined as

$$R = \frac{1}{N}\sum_{j=1}^{N}\left(\frac{sI_j^c - I_j^o}{I_j^o}\right)^2 \tag{7}$$

is minimized, where I_j^o and I_j^c are the observed intensity and the calculated $|F|^2$, respectively, at point j in the reciprocal

TABLE I. Optimized parameters of surface atoms of the [Al/MgO]$_1$ truncation model, where Sc atom marked with + in Fig. 1 is set at the origin of the atomic coordinate Z. $U_{11}{}^{1/2}$ and $U_{33}{}^{1/2}$ of surface O1 were not optimized.

Atom	Occupancy	Z/c	$U_{11}{}^{1/2}$ (Å)	$U_{33}{}^{1/2}$ (Å)
Al/Mg	1.00(4)	0.1156(7)	0.20(3)	0.13(7)
O1	0.85(6)	0.129(2)	0.2(fixed)	0.18(fixed)

TABLE II. Fractional atomic coordinates z of bulk atoms in the unit of c obtained at 298 K by this work and references, where Sc atom is set at the origin and atoms aligning along c-axis are listed. As a result, Z/c in Table I and Fig. 6 is identical with z for O1 and with $1/3 - z$ for Al/Mg and O2.

Atom	This work	a	b	c
Sc	0	0	0	0
Al/Mg	0.2173(6)	0.21630(2)	0.216453	0.217(1)
O1	0.128(3)	0.12791(7)	0.127713	0.128(1)
O2	0.293(1)	0.29276(6)	0.293008	0.293(1)

[a]Powder diffraction at 323 K of Ref. 3.
[b]Single-crystal diffraction at room temperature of Ref. 2.
[c]Powder diffraction at room temperature of Ref. 2.

space, and N is the number of the measured points. The scale factor s common to all rods is calculated as

$$s = \sum_{j=1}^{N} \left(I_j^c / I_j^o\right) / \sum_{j=1}^{N} \left(I_j^c / I_j^o\right)^2 \qquad (8)$$

for each of the parameter set. The R-factor is minimized by using the Levenberg-Marquardt method for least-squares fit. U_{11} and U_{33} (MSDs) of bulk atoms are fixed at the values in Table III. These values are obtained by least-square fit of the temperature dependence of MSDs in Ref. 3 to the Einstein model of thermal vibration[4,20] with additional constant of a stationary MSD U_0. U_0 is necessary for the fitting owing to the random distribution of Al and Mg; U_0 is largest for U_{11} of the O1 atom, which is located next to Al/Mg. Also U_{11} and U_{33} of the surface O atom could not be optimized by the R-factor minimization method because these two parameters were optimized to a physically anomalous value of zero as shown in Fig. 6(a). Instead, as shown in Fig. 6, its ${U_{11}}^{1/2}$ is fixed at 0 (black lines), 0.15 (blue lines), 0.2 (red lines), and 0.25 Å (green lines). Its ${U_{33}}^{1/2}$ is fixed at one of the 16 values along the horizontal axes in Fig. 6 during the optimization of other parameters. The decrease in MSDs of surface O atom has strong correlation with the decrease in its occupancy as shown in Fig. 6(b). Moreover, parameters of O atom are generally difficult to be estimated because its atomic scattering factor is smaller than that of the other elements in $ScAlMgO_4$ (see the supplementary material).

${U_{11}}^{1/2}$ and ${U_{33}}^{1/2}$ (RMSDs) of bulk O1 at 298 K are 0.155 and 0. 134 Å, respectively, from Table III. RMSDs at the surface are usually larger than those in bulk owing to the

TABLE III. U_{11} and U_{33} of bulk atoms at 298 K obtained by least-square fit of the temperature dependence of MSD in Ref. 3, where fitting parameters are stationary mean-square displacement U_0 and Einstein temperature Θ.

Atom	ii	U_{ii} (Å^2)	U_0 (Å^2)	Θ (K)
Sc	11	0.0071(2)	0.0035(2)	316(6)
	33	0.0165(5)	0.0090(5)	212(4)
Al/Mg	11	0.0074 (5)	0.0032(4)	387(11)
	33	0.0111(7)	0.0061(6)	353(12)
O1	11	0.0240(6)	0.0175(5)	399(8)
	33	0.0180(1)	0.01114(9)	389(2)
O2	11	0.0093(6)	0.0038(6)	440(14)
	33	0.0107(4)	0.0065(3)	513(12)

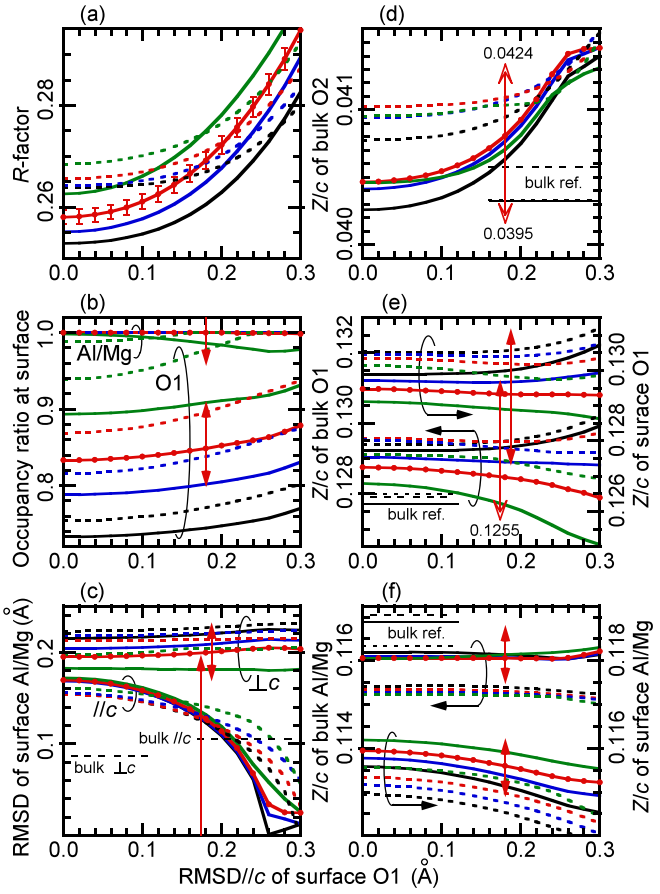

FIG. 6. Variations of the minimized R-factor and optimized parameters of the $[Al/MgO]_1$ truncation model as a function of root-mean-square displacement (RMSD) ${U_{33}}^{1/2}$ of surface O1 atom. Distinction between O1 and O2 atoms is indicated in Fig. 1. Results using atomic scattering factors of neutral atoms (dashed lines) and ions (solid lines) are shown. ${U_{11}}^{1/2}$ of surface O1 is fixed at 0 (black), 0.15 (blue), 0.2 (red), and 0.25 Å (green). Each vertical arrow indicates the range where R-factor is smaller than 0.285 as a measure of estimation error of the optimized parameter. Horizontal lines indicate reference values of bulk parameters of Ref. 3 (long dashed lines), single-crystal diffraction of Ref. 2 (solid lines), and powder diffraction of Ref. 2 (short dashed lines). Atomic Z/c coordinates of Al/Mg and O2 correspond to $1/3 - z$ of the references.

softening of the thermal vibrations by the break in bonds. However, the minimized R-factor monotonically increases with RMSDs of surface O atom as shown in Fig. 6(a). Furthermore, when ${U_{33}}^{1/2}$ of surface O atom is larger than about 0.2 Å, estimated ${U_{33}}^{1/2}$ of surface Al/Mg becomes smaller than that of bulk as shown in Fig. 6(c). Therefore, parameters optimized under fixed ${U_{11}}^{1/2}$ and ${U_{33}}^{1/2}$ of surface O atom at 0. 2 and 0.18 Å, respectively, are listed in Tables I and II as the most proper estimation. Both of the fixed RMSDs are about 1.3 times of the bulk ones. Blue solid lines in Fig. 3 show CTR curves at the optimized parameters. The agreement about the position and shape of the deep dips between the observation and the calculation is refined. The error bars in Fig. 6(a) indicate the error of R-factor estimated from the statistical error of the observed intensities. However, at least the lowest R-factor obtained for the zero RMSD of surface O should be in the range of a proper error of R-factor. The vertical arrows in Fig. 6 indicate the ranges where R-factor is smaller than 0.285 when only the single parameter of each vertical axis is moved while other

parameters are fixed at the optimum values. The range of each arrow is regarded as a measure of estimation error of the optimum parameter, and is shown in Tables I and II.

$U_{11}{}^{1/2}$ ($U_{33}{}^{1/2}$) of surface Al/Mg is estimated as 0.20 (0.13) Å, which is about 2.3 (1.2) times of the bulk value in Table III. This is explained well by the stationary in-plane displacements of the surface Al/Mg atoms, which are enhanced by the partial desorption of surface O atoms during the thermal cleaning. The in-plane position of a surface Al/Mg atom is probably displaced from the symmetric position toward randomly created surface O vacancies. Therefore, the large $U_{11}{}^{1/2}$ of surface Al/Mg and the reduced surface O occupancy ratio look consistent with each other. Furthermore, the Al/MgO layers in $ScAlMgO_4$ are probably compressed along *c*-plane, which is suggested by the rumpling of alternate Al/Mg and O atoms compared with the flat h-BN layer. On the other hand, the ScO_2 layers are probably tensed, which is suggested by the distorted bond angles around Sc atom from the rocksalt-like right angle as shown in Fig. 1. These distortions may be caused by the alternate stacking of layers with different own in-plane lattice constants. If this is the case, the partial desorption of the surface O atom is favorable to release the strain. The deficiency of surface O atom is also consistent with the appearance of the electrical conduction, which suppressed the charge up during the RHEED observation, only after the thermal cleaning. It is also considered that the surface O site is fully occupied just after the cleavage because RHEED observation is not possible owing to the charge up. The optimized occupancy of the surface Al/Mg is almost unity. This suggests that carriers are electrons from the excess Al/Mg atoms. It is predicted by the bulk band calculations that conduction band minimum of $ScAlMgO_4$ is located in the ScO_2 layer.[11] However, surface states localized at the excess Mg/Al atoms are considered to appear in the band gap and some of the electrons are excited to the conduction band in nearby ScO_2 layers. In the CTR calculations, the excess Al/Mg atoms are assumed to be neutral to maintain the consistency of the total electron numbers at the surface. The optimized parameters in Tables I and II suggest that the surface O (Al/Mg) atom is displaced 0.02 ± 0.09 (-0.01 ± 0.02) Å to vacuum from the ideal bulk-truncated position. This may be related to the formation of *s*-like lone pair and increase in *p*-like component in the back bonds of the surface O atoms. However, the estimated displacement is smaller than its error. Thus, we can only conclude that the surface atoms are located nearly at their bulk-truncation positions and only their scattering factors are reduced from those in bulk owing to the increased RMSDs of the surface O and Al/Mg atoms, and the reduced occupancy of the surface O atom.

The Ga-polar *c*-plane GaN grows on a thermally cleaned cleaved $ScAlMgO_4$ by MOVPE.[4] Our conclusion of the oxygen deficiency looks consistent with this experimental result because oxygen deficient $ScAlMgO_4$ surface probably has excess electrons. The ideal surfaces of N-polar and Ga-polar GaN have dangling bonds of surface N and Ga atoms, respectively. The energy level of the N dangling bond is lower than that of the Ga dangling bond owing to the difference in their electronegativity. Then, the N-polar inner surface is preferred at the interface formation with the oxygen deficient $ScAlMgO_4$ surface because the excess electrons from $ScAlMgO_4$ can be transferred to fill the lower energy N dangling bonds of GaN. In addition, surface energy of the hydrogenated Ga-polar surface is lower than that of the N-polar surface.[21] This also assists the Ga-polar surface to be the outer surface of GaN.[22] The cleaved $ScAlMgO_4$ surface was cleaned in H_2 flow at 1005 °C for 8 min before the MOVPE growth of GaN.[4] Therefore, much more significant oxygen deficiency is presumable. On the other hand, O-polar ZnO grows on a polished $ScAlMgO_4$.[23] This result is probably attributed to the oxygen atmosphere, which prevents the oxygen deficiency of the $ScAlMgO_4$ surface, during the ZnO growth. As for the MOPVE grown GaN, further studies on the $ScAlMgO_4$ surface after the H_2 cleaning and the interface atomic structure between $ScAlMgO_4$ and GaN are required to fully clarify the polarity selection mechanism.

C. Electrostatic energy barrier and mechanism of the cleavage

Though the bond length between the two Al/MgO layers is 0.3 Å longer and each bond is probably weaker than that between the Al/MgO and ScO_2 layers, the bond density of the former interlayer is twice of that of the latter interlayer. In order to understand the reason why $ScAlMgO_4$ is cleaved between the two Al/MgO layers, the impact of electrostatic-energy change during the separation is compared between the two interlayers. To estimate the electrostatic-energy change, a cylindrical block of *c*-plane $ScAlMgO_4$ (both of thickness and diameter are $82c/3$) is cleaved at its half thickness. It is assumed that the ionic charges of Sc, Al/Mg, and O are $+3, +2.5$, and -2, respectively. The electrostatic potential energies between all ion pairs are summed up. However, to evaluate the change in the energy during the separation of the cleaved two blocks, the potential energies between ion pairs within the same block can be omitted. Furthermore, the lower block consisting only of a 1×1 column along the cylindrical axis is enough and even yields more accurate result than the cylindrical lower block.

In Fig. 7, changes in the electrostatic energy per 1×1 area as a function of the moving distance of the upper block along *c*-direction are shown. The topmost *c*-plane of the upper cylinder and the bottom of the lower column are terminated by $[Al/Mg\text{-}O]_1$ to avoid *c*-axis dipole electric field in the $ScAlMgO_4$ before the cleavage. After the cleavage, the topmost surface of the lower column is truncated at $[Al/Mg\text{-}O]_1$ (solid lines) or $[ScO_2]$ (dashed lines). The energy change for the $[ScO_2]$ truncation at large separation distance d is approximated by an analytical potential energy

$$U(d) = \frac{e^2}{4\sqrt{3}a^2\varepsilon_0}\left(d - \sqrt{R^2 + d^2}\right) \tag{9}$$

between a circular-sheet charge, whose radius is R and charge density is $e/2$ per 1×1 area, and a point charge of $-e/2$ at distance d on the cylindrical axis, where ε_0 is the vacuum permittivity. The inset of Fig. 7 shows the changes in much wider range of the distance for the ionic model of the $[ScO_2]$ truncation (red dashed line) and the analytical energy (blue dots), which is a good approximation of the ionic model.

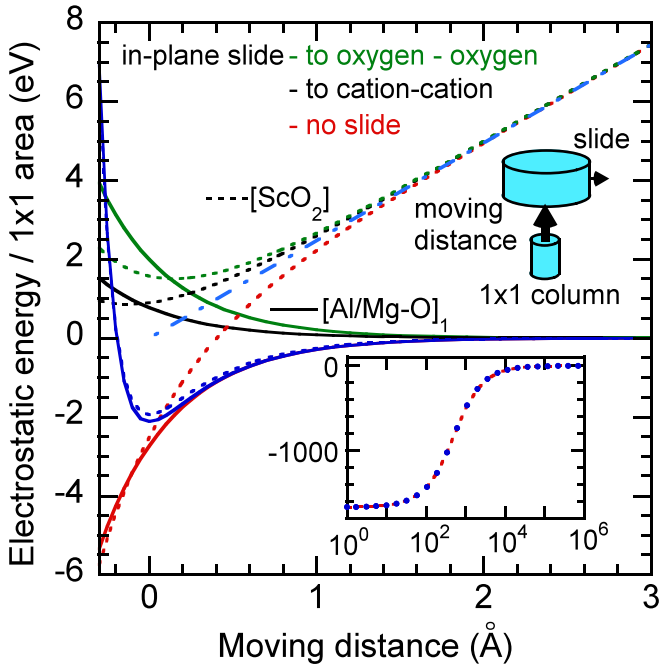

FIG. 7. Electrostatic-potential-energy changes between all ion pairs in the upper cylindrical block and the lower 1×1 column of $ScAlMgO_4$ as a function of the moving distance of the upper block along c-direction. The lower column is truncated at $[Al/MgO]_1$ (solid line) or $[ScO_2]$ (dashed line) with no in-plane slide (red line), slide to cation-cation c-alignment at the interface (black line), and to oxygen-oxygen alignment (green line). The dashed lines are vertically shifted 1664.14 eV to cancel the potential energy shift in the inset, where variation in much wider range of the distance for the $[ScO_2]$ truncation (red dashed line) and analytical potential energy between circular-sheet charge and point charge (blue dots) are shown. After the shift, the energy changes for the $[ScO_2]$ truncation converge to that for a parallel-plate capacitor (chained line). The blue lines indicate schematic bonding-potential curve with the introduction of an exponentially-decreasing repulsive potential.

When $d \gg R$, $U(d)$ approaches to the energy between two point charges. When $d \ll R$, $U(d)$ approaches to the energy of a parallel-plate capacitor with an additional constant proportional to R because zero level of the potential energy is set at infinitely separated state of the two blocks. To offset the additional constant, the curves for the $[ScO_2]$ truncation in the main plot of Fig. 7 are vertically shifted 1664.14 eV. After the shift, the curves for the $[ScO_2]$ truncation converge to the electrostatic energies of the parallel-plate capacitor with surface charges $\pm e/2$ per 1×1 area (chained line) above the distance 2 Å. Three cases of the separation (i) without in-plane slide (red line), (ii) after slide to cation-cation c-alignment at the interface (black line), and (iii) after slide to oxygen-oxygen c-alignment (green line), are examined for each truncation. The oxygen-oxygen alignment is obtained by $(\mathbf{a}_1 - \mathbf{a}_2)/3$ slide of the upper block for the $[Al/Mg\text{-}O]_1$ truncation and $(\mathbf{a}_2 - \mathbf{a}_1)/3$ slide of the upper block for the $[ScO_2]$ truncation, where $\mathbf{a}_1$ and $\mathbf{a}_2$ are the in-plane primitive translation vectors in Fig. 4. The cation-cation alignment is obtained by the opposite shift for each truncation. As shown in Fig. 7, the oxygen-oxygen alignment has larger repulsive energy owing to the smaller distance between the oxygen-oxygen than that between the cation-cation. The changes in the electrostatic energies converge irrespective of the in-plane slide above the distance larger than about 2 Å. To obtain the convergence of the calculations at a relatively small size of the blocks, it is important that all of the atomic layers in the upper block have the same number of ions. To assure the adequacy of the block size, it was also confirmed that the half-height blocks and half-diameter upper block gave the same results as the main plot of Fig. 7. The curves in the inset depend on the diameter given in Eq. (9).

Among the six cases in Fig. 7, the separation between the two Al/MgO layers without in-plane slide undergoes the smallest barrier. Even if the surface charges of the $[ScO_2]$ truncation are neutralized by tunneling or discharge at a certain distance larger than about 1 Å and the parallel-plate-capacitor-like component disappears, the barrier for the cleavage is higher than that between the two Al/MgO layers. Therefore, the cleavage induced by the impact of the razor blade probably happens in the way of red solid line in Fig. 7. However, the self-cleavage of $ScAlMgO_4$, which is caused by the in-plane stress due to the mismatch of the thermal expansion coefficient between thick c-GaN epitaxial film and $ScAlMgO_4$ substrate and the resultant wafer bowing,[10] probably starts from the in-plane slides. This is because atoms are freely displaced in c-direction until the stress in this direction is relaxed. The in-plane slide, along the central plane of the Al/MgO bilayer near the interface with GaN, starts from the side edge of the $ScAlMgO_4$ substrate in order to release the in-plane stress. The slid area gets free from both the stress and the bowing. In this process, part of the released strain energy is used to lift the interface energy between the two slid Al/MgO layers because these layers become incommensurate to each other. Here, the in-plane lattice constant of the thin $ScAlMgO_4$ that remains at the bottom of the thick GaN is not relaxed. As a result, the regions of the oxygen-oxygen and the cation-cation alignments, where the interlayer force between the Al/MgO bilayer is repulsive, and the normally stacking region, where the interlayer force is attractive, and intermediate regions between them are periodically repeated. The period is estimated to be about 600 nm when the in-plane strain due to the difference in the lattice contraction between $ScAlMgO_4$ and GaN during cooling is 0.05%.[4] It is considered that $ScAlMgO_4$ is easily separated between the two completely slid and weakly bonded Al/MgO bilayer.

The blue lines in Fig. 7 indicate schematic interlayer potential energy curves per 1×1 area with an introduction of the exponentially-decaying repulsive potential,[24] whose repulsive range parameter is set at 0.1 Å and strength is adjusted to let the potential reach minimum at the distance zero. The parallel-plate-capacitor-like component of the $[ScO_2]$ truncation is subtracted. The depth of the potential for the two truncations, where there are two and one broken bonds per 1×1 area respectively for the $[Al/MgO]_1$ and $[ScO_2]$ truncations, is nearly the same by this simple estimation. Therefore, the inversion symmetry in the $[Al/MgO]_1$ truncated $c/3$ block, which cancels the electric dipole moment and surface charge, is probably a more important factor to be the cleavage position than the 0.3 Å longer bond length at this interlayer. Monatomic crystal of the diamond-type Si is cleaved along the (111) plane because the dissociated bond density is the smallest in this plane. However,

compound crystal of the zincblende-type GaAs is cleaved along the (110) plane, where the dissociated bond density is $(3/2)^{1/2}$ times larger than that of the (111) plane. This is because electric dipole moment perpendicular to the (110) plane is zero. Furthermore, the wurtzite-type GaN is cleaved along the $(10\bar{1}0)$ plane and the rocksalt-type MgO is cleaved along the (001) plane, where surface-normal electric dipole moments are also zero. In these compounds, each atomic layer parallel to the cleavage plane is neutral. On the other hand, $ScAlMgO_4$ is not neutral in the atomic layer level. However, both neutrality and zero electric dipole moment in the c/3 unit are fulfilled by the $[Al/MgO]_1$ truncation. As a result, the separation of the two parts truncated with $[Al/MgO]_1$ does not suffer the parallel-plate-capacitor-like attractive electrostatic force. Therefore, cleavage of $ScAlMgO_4$ between the two Al/MgO layers is quite reasonable.

IV. CONCLUSIONS

It is revealed by the X-ray CTR scattering method that $ScAlMgO_4$ is cleaved between the two Al/MgO layers. The bonds between the two Al/MgO layers are weaker due to 16% longer bond length than the bonds between the Al/MgO and the ScO_2 layers. However, this weak-bond effect is almost canceled by the double-density bonds of the former interlayer. More important cause of the cleavage between the two Al/MgO layers is that the two separated parts are inversion symmetric to each other and no surface charges are left on the cleaved surfaces. In this case, parallel-plate-capacitor-like electrostatic attractive force is prevented during the separation process. About 10% to 20% of the oxygen atoms at the topmost layer of the cleaved surface desorb after the 18-min cleaning at 600 °C in UHV. This induces excess electron carriers at the $ScAlMgO_4$ surface. From the surface oxygen deficiency, a possible mechanism was proposed for the polarity selection of *c*-GaN grown on the cleaved and thermally cleaned $ScAlMgO_4$. Two types of cleavage are currently known: one is caused by the impact of a wedge and the other is caused by the in-plane stress induced by the thermal-expansion mismatch with an overgrown thick GaN film. The difference between the two cleavage processes was discussed based on the electrostatic potential energy. $ScAlMgO_4$ has been used as a lattice-matching substrate for GaN, InGaN, and ZnO. In addition, $ScAlMgO_4$ and some of the related layered multicomponent oxides[1,11] are probably expected as a good substrate for the van der Waals epitaxy of two-dimensional materials. This is because the cleaved surface of $ScAlMgO_4$ has extremely wide terraces and the ideal Al/MgO truncated surface is terminated with fully occupied oxygen lone pairs. An oxidizing atmosphere during the surface cleaning probably protects the surface from the oxygen deficiency and provides a stable, chemically inert, and insulating surface.

SUPPLEMENTARY MATERIAL

See supplementary material for the plot of calculated CTR intensities of the truncations shown in Fig. 1 other than the $[Al/MgO]_1$ truncation.

ACKNOWLEDGMENTS

The X-ray measurements were performed at the BL13XU of SPring-8 with an approval of the Japan Synchrotron Radiation Research Institute (JASRI) (Proposal No. 2014B1463). The atomic structure in Fig. 1 was drawn by VESTA.[25]

[1]N. Kimizuka and T. Mohri, J. Solid State Chem. **78**, 98 (1989).
[2]D. Errandonea, R. S. Kumar, J. Ruiz-Fuertes, A. Segura, and E. Haussuhl, Phys. Rev. B **83**, 144104 (2011).
[3]R. Simura, K. Sugiyama, A. Nakatsuka, and T. Fukuda, Jpn. J. Appl. Phys. **54**, 075503 (2015); **55**, 099201 (2016).
[4]T. Iwabuchi, S. Kuboya, T. Tanikawa, T. Hanada, R. Katayama, T. Fukuda, and T. Matsuoka, Phys. Status Solidi A **214**, 1600754 (2017).
[5]E. S. Hellman, C. D. Brandle, L. F. Schneemeyer, D. Wiesmann, I. Brener, T. Siegrist, G. W. Berkstresser, D. N. E. Buchanan, and E. H. Hartford, MRS Int. J. Nitride Semicond. Res. **1**, 1 (1996).
[6]A. Ohtomo, K. Tamura, K. Saikusa, K. Takahashi, T. Makino, Y. Segawa, H. Koinuma, and M. Kawasaki, Appl. Phys. Lett. **75**, 2635 (1999).
[7]A. Tsukazaki, A. Ohtomo, T. Onuma, M. Ohtani, T. Makino, M. Sumiya, K. Ohtani, S. F. Chichibu, S. Fuke, Y. Segawa, H. Ohno, H. Koinuma, and M. Kawasaki, Nat. Mater. **4**, 42 (2005).
[8]T. Ozaki, Y. Takagi, J. Nishinaka, M. Funato, and Y. Kawakami, Appl. Phys. Express **7**, 091001 (2014).
[9]T. Ozaki, M. Funato, and Y. Kawakami, Appl. Phys. Express **8**, 062101 (2015).
[10]K. Ohnishi, M. Kanoh, T. Tanikawa, S. Kuboya, T. Mukai, and T. Matsuoka, Appl. Phys. Express **10**, 101001 (2017).
[11]A. Murat and J. E. Medvedeva, Phys. Rev. B **85**, 155101 (2012).
[12]E. Vlieg, J. Appl. Cryst. **33**, 401 (2000).
[13]T. P. Trainor, P. J. Eng, G. E. Brown, Jr., I. K. Robinson, and M. De Santis, Surf. Sci. **496**, 238 (2002).
[14]V. M. Kaganer, Phys. Rev. B **75**, 245425 (2007).
[15]O. Sakata, Y. Furukawa, S. Goto, T. Mochizuki, T. Uruga, K. Takeshita, H. Ohashi, T. Ohata, T. Matsushita, S. Takahashi, H. Tajiri, T. Ishikawa, M. Nakamura, M. Ito, K. Sumitani, T. Takahashi, T. Shimura, A. Saito, and M. Takahasi, Surf. Rev. Lett. **10**, 543 (2003).
[16]E. Vlieg, J. Appl. Cryst. **30**, 532 (1997).
[17]E. Vlieg, J. Appl. Cryst. **31**, 198 (1998).
[18]D. T. Cromer and J. T. Waber, in *International Tables for X-Ray Crystallography*, edited by J. A. Ibers and W. C. Hamilton (Kynoch Press, Birmingham, 1974), Vol. IV.
[19]S. Sasaki, KEK Rep. **88-14**, 1 (1989), see http://www.iaea.org/inis/collection/NCLCollectionStore/_Public/20/081/20081580.pdf.
[20]M. Schowalter, A. Rosenauer, J. T. Titantahb, and D. Lamoen, Acta Crystallogr., A **65**, 227 (2009).
[21]C. E. Dreyer, A. Janotti, and C. G. Van de Walle, Phys. Rev. B **89**, 081305(R) (2014).
[22]H. Nakane, T. Akiyama, K. Nakamura, and T. Ito, J. Cryst. Growth **468**, 93 (2017).
[23]B. Wessler, A. Steinecker, and W. Mader, J. Cryst. Growth **242**, 283 (2002).
[24]C. Kittel, *Introduction to Solid State Physics*, 8th ed. (John Wiley & Sons, New Jersey, 2005), p. 60.
[25]K. Momma and F. Izumi, J. Appl. Cryst. **44**, 1272 (2011).